Volume 14
Number 36
28 September 2022
Pages 12953-13390

Nanoscale

rsc.li/nanoscale

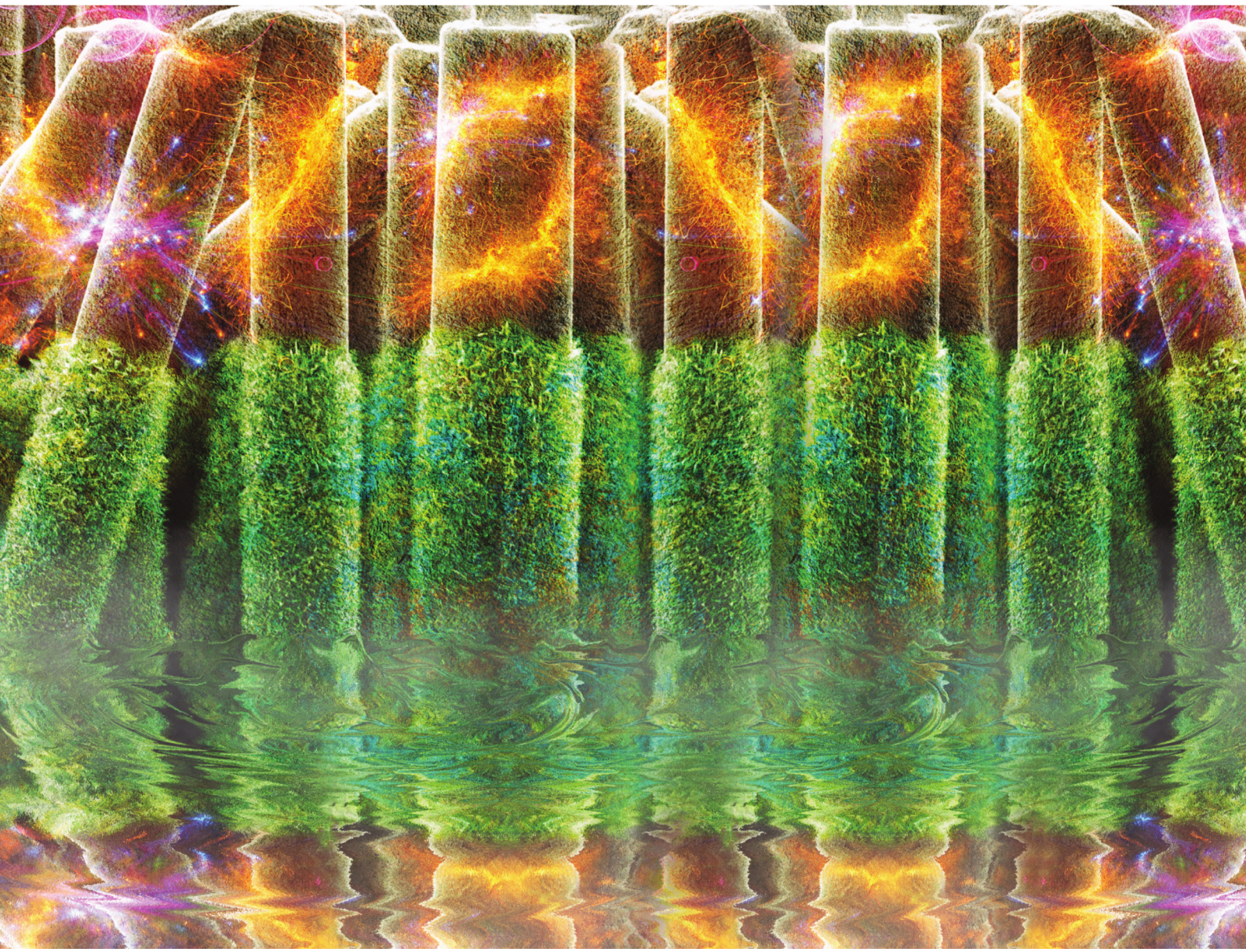

ISSN 2040-3372

ROYAL SOCIETY OF CHEMISTRY

NCNST

Nanoscale

PAPER

View Article Online
View Journal

Cite this: DOI: 10.1039/d2nr02447k

Computer vision-assisted investigation of boiling heat transfer on segmented nanowires with vertical wettability†

Jonggyu Lee,‡[a] Youngjoon Suh, ‡[a] Max Kuciej,[b,c] Peter Simadiris,[a] Michael T. Barako[c] and Yoonjin Won *[a,d]

The boiling efficacy is intrinsically tethered to trade-offs between the desire for bubble nucleation and necessity of vapor removal. The solution to these competing demands requires the separation of bubble activity and liquid delivery, often achieved through surface engineering. In this study, we independently engineer bubble nucleation and departure mechanisms through the design of heterogeneous and segmented nanowires with dual wettability with the aim of pushing the limit of structure-enhanced boiling heat transfer performances. The demonstration of separating liquid and vapor pathways outperforms state-of-the-art hierarchical nanowires, in particular, at low heat flux regimes while maintaining equal performances at high heat fluxes. A deep-learning based computer vision framework realized the autonomous curation and extraction of hidden big data along with digitalized bubbles. The combined efforts of materials design, deep learning techniques, and data-driven approach shed light on the mechanistic relationship between vapor/liquid pathways, bubble statistics, and phase change performance.

Received 5th May 2022,
Accepted 16th August 2022

DOI: 10.1039/d2nr02447k

rsc.li/nanoscale

Introduction

Heat transfer surfaces for boiling exhibit a tradeoff between achieving high boiling efficacy and upper boiling limits.[1] The boiling heat transfer efficacy is typically quantified by the heat transfer coefficient (HTC), which relates the superheat temperature to the bubble activity-induced interfacial heat flow, and the critical heat flux (CHF), which establishes the upper limit of boiling heat flux as limited by liquid delivery.[2–10] To perform well on both aspects an ideal boiling surface must reconcile the competing demands for vapor production/extraction and liquid transport.[11]

According to classical nucleation theory, traditional homogeneous wicks have often been construed to be limited to either high-heat flux applications or low-heat flux, high-performance applications because they must compromise between bubble nucleation and departure.[12,13] Since bubble nucleation is governed by the interfacial activation energy barriers required for bubbles to form on the heated surface,[12,13] surfaces that favor bubble nucleation typically possess high surface roughness and intrinsic wettability.[8,9,12–14] However, these surface properties can have negative effects on vapor removal, hence limiting liquid delivery to the heated surface.[15] For example, past work shows that rough hydrophobic surfaces exhibit high HTC at low heat flux regions, but are plagued with low CHF due to delayed contact line movement and bubble overpopulation.[16] On the other hand, hydrophilic surfaces or wicking surfaces show superior CHF by preventing dry-out of the heated surface at high heat flux regions, but suffer from low HTC at low heat flux regions due to the large activation energy barriers for bubble nucleation.

In response to the boiling dilemma, modern boiling surfaces employ heterogeneous surface properties as a multifaceted approach to ensure favorable bubble dynamics and efficient liquid/vapor pathways.[17–22] A common research thrust is to utilize hydrophilic, micro/nano hierarchically enhanced surfaces with two or even multiple length scales.[23–28] These multi-tier-roughness surfaces achieve some of the highest reported boiling performances, which is attributed to the activation of more nucleation sites, effective evaporative surface area increase, and capillary-assisted surface rewetting enhancement.[1,25,27,29,30] Another effective approach recently receiving attention is the use of surfaces with opposing wettability.[15,23,31–35] This method capitalizes on the juxtaposi-

[a]Department of Mechanical and Aerospace Engineering, University of California, Irvine, Irvine, CA, 92697, USA. E-mail: won@uci.edu
[b]Department of Material Science and Engineering, University of California, Los Angeles, Los Angeles, CA, 90095, USA
[c]NG Next, Northrop Grumman Corporation, Redondo Beach, CA, 90278, USA
[d]Department of Electrical Engineering and Computer Science, University of California, Irvine, Irvine, CA, 92697, USA
†Electronic supplementary information (ESI) available. See DOI: https://doi.org/10.1039/d2nr02447k
‡These authors contributed equally.

tion of high and low activation energies to promote bubble nucleation on designated spots while continuously replenishing the rest of the surface with liquid.[15,36] To date, spatially mixed wettabilities have been realized by installing hydrophobic islands on hydrophilic surfaces,[15] or through stochastic deposition techniques,[37] which, in turn, have limited surface wetting areas.[23] Therefore, this study pursues the rational question of whether the advantages of hierarchical structures and biphilic surface properties can be combined and fine-tuned to maximize boiling heat transfer performances. To answer this question, it is imperative to build a strong mechanistic connection of surface property effects on boiling efficacy.[38] The mechanistic investigation of the highly intertwined relationship between surface properties and boiling heat and mass transfer, in turn, requires a rigorous analysis of bubble dynamics.

To quantify the collective bubble evolution behavior crucial for understanding boiling heat transfer mechanisms, we develop a vision-based framework that extracts in situ bubble features at single-bubble resolutions. Typically, a boiling surface emits hundreds of bubbles per second that individually exhibit complex movements, interactions, and morphologies, even near the onset of nucleate boiling (ONB), which poses a challenge for researchers to consistently annotate and track them.[38] Furthermore, high-level boiling features such as departure bubble diameter, departure frequency, and nucleation site density require connecting individual features throughout time. Therefore, an optical measurement taken at 2000 fps could easily translate to ⍰10^5 features per second. That is, the sheer volume of information from a single experiment makes manual bubble analysis methods difficult to capture representative bubble dynamic trends. Our deep learning framework, further referred to as Vision-Inspired Online Nuclei Tracker (VISION-iT), is customized to digitalize and recognize bubble instances in every frame and to autonomously extract rich bubble features from massive datasets that adequately represent the boiling system.[38,39]

Motivated by the promise of heterogeneous structures and empowered by the new vision-based characterization method, here we suggest using vertically aligned hierarchical nanowire (NW) arrays as boiling wicks, where each NW contains biphilic segments. The base segment is composed of a previously-published superhydrophilic CuO NW array,[29] which expeditiously draws liquid to the heated surface and facilitates bubble departure. The top segment is comprised of a hydrophobic Ni NW array that lowers the local activation energy barriers, thereby promoting bubble nucleation and triggering faster system transitions to the more efficient nucleate boiling region. The NW segments are vertically juxtaposed to fully separate vapor/liquid pathways, thereby segregating bubble activity and liquid transport functions for maximized HTC and CHF. We characterize the liquid transport and corresponding boiling heat transfer, which depends on the NW compound ratio and order. We then correlate the boiling performances with physical features that are extracted by VISION-iT. Our work not only reveals the undiscovered impact of heterogeneous wettability on pool boiling heat transfer, but also offers characterization methods that realize the autonomous curation and extraction of hidden big data residing within visual imagery.

Results

Segmented nanowire concept and design

To better design boiling curves, we propose a segmented NW design where the region adjacent to the interface is superhydrophilic whereas the region at the top of the surface is rough and hydrophobic, thus segregating the optimal properties to their respective regions (Fig. 1). The segment materials (Cu and Ni) are selected based on thermal conductivity (398 W m^{-1} K^{-1} for Cu and 106 W m^{-1} K^{-1} for Ni), intrinsic contact angle (⍰68° for Cu and ⍰101° for Ni), availability for electrochemical deposition, and corrosion resistance. The NWs are rendered biphilic by decorating the Cu portion with superhydrophibic CuO nanofeatures via selective oxidation. Unlike most spatially patterned biphilic boiling surfaces, our segmented NW design maximizes the projected surface area for liquid drawing and bubble nucleation by vertically aligning portions with opposing wettabilities. The hydrophobic Ni NWs nucleate bubbles at higher densities than the superhydrophilic CuO NWs at lower superheats due to low bubble activation energy and high density of entrapped vapor sites (Fig. 1a). At the same time, the large contact angle of the Ni NWs hinders bubble departure such that neighboring nucleation sites are forced to merge before departure. In contrast, the hydrophilic CuO NWs have slightly delayed ONB points, but quickly release bubbles from the surface once they form. Furthermore, liquid is more easily replenished to the heated surface through the water-friendly CuO NWs, compared to the Ni NWs (Fig. 1b). We postulate that our proposed design will combine the advantages of both Ni and CuO NWs, thereby possessing both favorable bubble dynamics and higher dry-out thresholds (Fig. 1c).

To experimentally reconcile our hypothesis, we fabricate a series of NWs with varying composition ratios and orders as shown in Fig. 2a–c. Singular NWs are denoted using their primary materials (e.g., Ni NWs, CuO NWs), whereas segmented NWs are additionally labeled by the portion order. For example, CuO/Ni indicates that the CuO compound is on the top, while the Ni element is on the bottom portion of the segmented NWs, and vice versa (Fig. 2c). The NWs are prepared via electrodeposition techniques using porous sacrificial templates (see Experimental section for details).[40,41] Based on our previous work on hierarchical CuO NWs,[29] we select an optimal template pore diameter of 1000 nm that renders NWs with high permeability and capillary pressure. By tuning the electrodeposition time and element order, we fabricate NWs with near-constant length ($l_{tot} \approx 21 \pm 2$ μm) but having varying composition ratios l_{CuO}/l_{tot} (see Fig. 2b, c and Table 1 to see the full list of the NWs). We note that we keep the NW length constant in order to isolate the effect of the segmented architectures on pool boiling performance in this study.

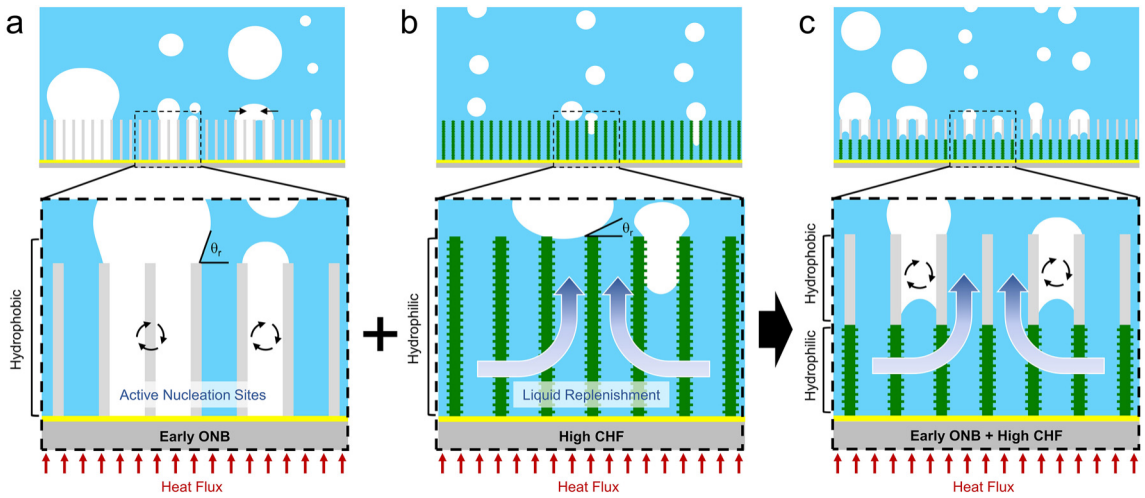

Fig. 1 Schematic of pool boiling mechanisms using segmented nanowires (NWs). The illustrations depict bubble nucleation/departure and liquid rewet-ting behaviors for various NW cases. (a) Hydrophobic NWs have low activation energy barriers, meaning that they are generally proficient at nucleating bubbles. Furthermore, the large rewetting angles allow for vapor entrapment in surface cavities, which become active nucleation sites. However, bubble departure is delayed due to delayed contact line motions, causing bubbles to merge before departure. (b) Hydrophilic NWs enable efficient liquid replen-ishment to the surface and delay the formation of resistive vapor blankets that lead to the surface dry-out. In contrast to hydrophobic surfaces, bubble nucleation is deterred due to high activation energies but are easily detached from the surface once they form. (c) The proposed segmented NW design aims to capitalize on the advantages of both low activation energy barriers and high liquid delivery through dual wettability.

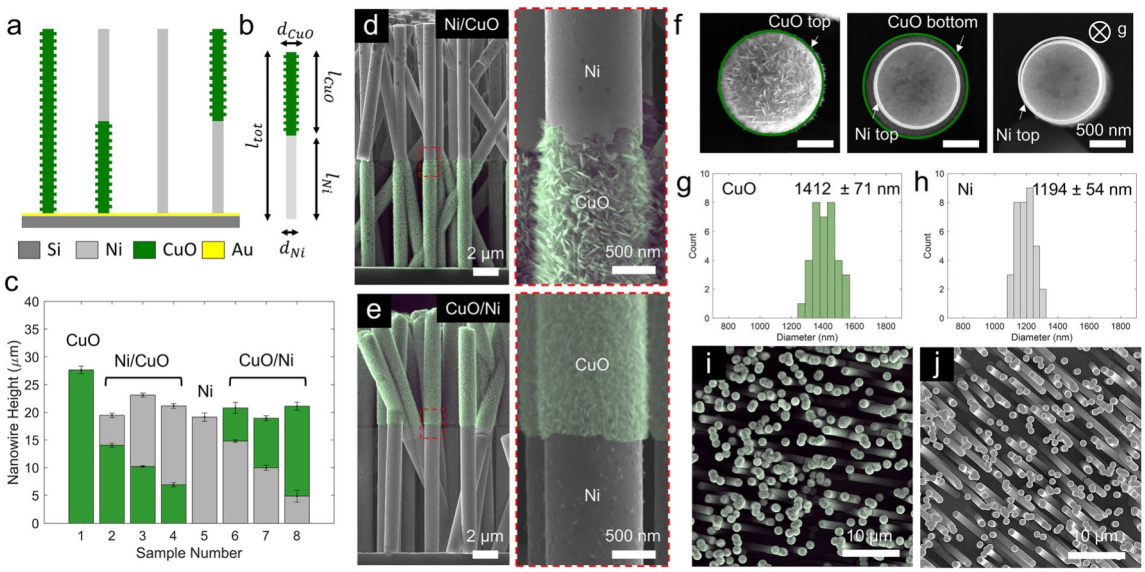

Fig. 2 Nanoscale morphologies of segmented NWs. (a) We classify our NWs into four categories and denote them based on their material and composition order. The figure illustrates CuO, Ni/CuO, Ni, and CuO/Ni NWs from left to right, respectively. (b) The NWs are further described by quantifying the CuO content, represented as CuO portion length to total length ratio l_{CuO}/l_{tot}, where $l_{tot} \approx 20$ μm for all NWs in this study. (c) The chart lists eight NW samples with varying composition ratios and order. The green and grey color represents CuO and Ni portion, respectively. Side-view scanning electron microscopy (SEM) images show the nanoscale morphology of segmented (d) Ni/CuO NWs (sample 3) and (e) CuO/Ni NWs (sample 7). (f) SEM images show the CuO/Ni, Ni/CuO, and Ni NWs, respectively. The top-view images clearly show selective diameter growth in por-tions where CuO nanofeatures are grown. The histograms show the distribution of nanowires' diameter of the (g) CuO portion and (h) Ni portion. SEM images of the wide top-view of the (i) CuO/Ni and (j) Ni/CuO NWs confirm minimal difference in terms of tortuosity, density, and orientation.

Nanoscale morphology

To introduce additional surface roughness, secondary CuO nanofeatures are selectively grown on the as-fabricated Cu portion of the NWs via chemical immersion (Fig. 2d and e). The targeted oxidation onto the Cu NWs produces dense, sharp CuO nanoscale features that selectively increase the local Cu NW diameters as shown in Fig. 2f–h. SEM images

Table 1 Summary of sample details for segmented nanowires after oxidation

Sample number	Segment type	l_{Cuo}/l_{tot}	φ	θ_{app} (°)
Sample 1	CuO	1.00	0.64	23.7
Sample 2	Ni/CuO	0.72	0.67	60.4
Sample 3	Ni/CuO	0.44	0.70	55.8
Sample 4	Ni/CuO	0.33	0.71	48.3
Sample 5	Ni	0	0.74	103.5
Sample 6	CuO/Ni	0.29	0.71	25.7
Sample 7	CuO/Ni	0.47	0.69	26.6
Sample 8	CuO/Ni	0.84	0.66	25.8

(Fig. 2f) clearly show that the Ni portion retains a smooth surface with negligible morphological changes, whereas the roughness and effective diameter of the CuO portion increases. It should be noted that Ni is corrosion resistant and is thereby unaffected by the chemical oxidation process. The segmented NW diameters are measured from side-view images (see Fig. S1† for details), where the distribution is shown in Fig. 2g and h. The average Ni NW and CuO NW diameter is measured as d_{Ni} = 1194 nm and d_{CuO} = 1412 nm, respectively. Since the chemical oxidation has no noticeable effects on the NW's natural tortuosity (Fig. 2i and j), the porosity becomes a function of the effective NW diameter, which differs for each segment. By factoring in the diameter differences between segments into porosity calculations, we report a porosity of 0.6 ± 0.05 across all NW samples. Please see ESI S1† for porosity calculation. We additionally report that the electrodeposition order decides the base material surface properties as well. To fabricate Ni/CuO NWs, the Cu material is deposited first, generating a very thin layer of Cu between the Au base and template. During the selective oxidation process, this thin layer becomes oxidized as well, reinforcing a superhydrophilic CuO base layer of ⍰400 nm as shown in Fig. S1.† By contrast, the Ni and CuO/Ni NW base do not show any level of oxidation.[42]

Nanostructure-coupled surface-liquid interactions

We investigate the intrinsic wettability effect on interfacial phenomena by performing a contact angle test on all surfaces (Fig. 3a). In comparison to the plain surface tests in Fig. S2 and S3† shows that the NWs containing Cu content significantly increase in hydrophilicity after chemical oxidation (60% < Δθ < 60%), regardless of the composition order. Please note that Δθ is the contact angle difference of the sample before and after chemical oxidation. In addition, Ni/CuO NW surface exhibits less severe contact angle drops compared to CuO/Ni and CuO NW surfaces (Fig. S3†), maintaining contact angles over 50° across all composition ratios. We note that the errors between different composition ratios all lie within one standard deviation (Fig. 3a). These findings not only highlight the extreme wettability bandwidth that hierarchical NWs possess,

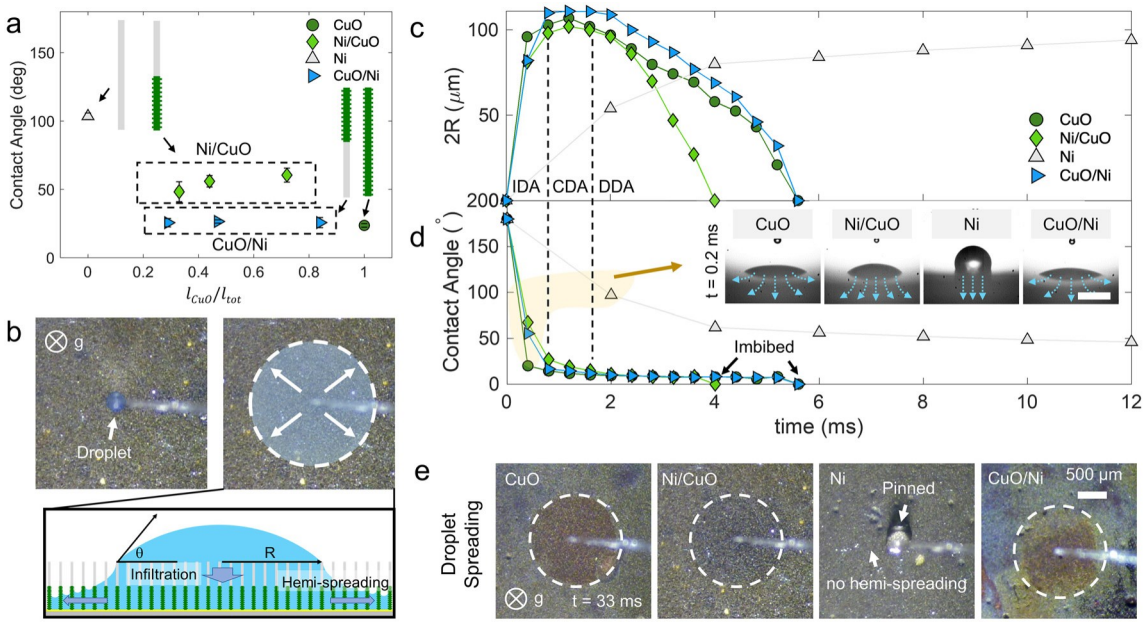

Fig. 3 Surface wetting characteristics of NWs. (a) The contact angles of segmented NWs are evaluated with the sessile drop method. Error bar represents one standard deviation. (b) Top-view optical images of a droplet spreading during the sessile drop test. The illustration shows the hemi-spreading of a droplet on top of a Ni/CuO NW array. The plots for the dynamic (c) diameter of the drawing area and (d) contact angle describe the full droplet imbibition process for representative NW cases, in which the segmented NW cases have $l_{CuO}/l_{tot} \approx 0.5$. Three distinct IDA, CDA, and DDA phases characterize the droplet imbibition. Contact angles are measured near the beginning of the CDA phase in the highlighted regions. The inset shows droplets on different samples in the highlighted regions, where liquid delivery pathways are illustrated in blue arrows. The scale bar represents ⍰170 μm. (e) The images show representative images of droplets spreading at t = 33 ms. The droplets on segmented NWs with CuO contents are fully imbibed, where spread marks are circled in white. The droplets on the Ni NWs, on the other hand, are pinned to the Au sample base. Light refraction-induced color changes can be used to characterize which portion of the NWs spreading occurs.

but also imply that the interfacial interactions are, to some degree, governed by the initial liquid–solid contact material.

To study how material composition order influences the wetting behavior, we observe droplet spreading via top view imaging. Once a sessile drop is placed on the NW array, the droplet is infiltrated into the pores and spreads via capillary actions in the radial direction as shown in Fig. 3b. This behavior is also known as "hemi-spreading"[43,44] and results from Cassie to Wenzel state transitions.[45,46] The hemi-spreading occurs when measured contact angles are smaller than the critical contact angle $\theta_c = \cos^{-1}(1 - \varepsilon)/(r - \varepsilon)$, where r is the roughness and ε is the solid fraction. In this computation, we assume NW arrays are aligned in hexagonal arrays, which gives $r = 1 + 2\pi dl_{tot}/\sqrt{3}p^2$, where the pitch between NWs is $p = d\sqrt{2/\sqrt{3}N}$. Accordingly, the critical contact angle is calculated as $\theta_c = 87°$ for r = 21 and p = 2240 nm, forecasting that hemi-spreading will occur for all nanowires with CuO components. Our experimental results agree well with the theoretical predictions, showing hemi-spreading behavior for all samples except for the Ni NW ($\theta > \theta_c$) sample (see Fig. S4† for top-view spreading images). Interestingly, we observe distinctive two-step spreading behaviors, characterized by light refraction-induced color changes during spreading events (Fig. S4†). The NW samples where CuO is the initial contact material to the falling droplet (Samples 1, 6–8) display high-contrast color changes, whereas the Ni/CuO samples (Samples 2–4) show little to no color changes. This implies that the droplet spreads immediately after liquid–solid contact on CuO-top NWs while following a vertical infiltration-to-spreading route for Ni-top NWs as illustrated in Fig. 3b. The sessile droplet retains more of its spherical shape when they meet hydrophobic Ni NWs, which explains why Ni/CuO NWs possess an overall higher contact angle than CuO/Ni NWs (Fig. 3a).

To verify that the microscopic liquid transport through the hierarchical CuO compounds governs interfacial phenomena, we observe additional droplet spreading via side-view imaging. Droplet spreading and imbibition into porous media can be analyzed by a classical liquid infiltration theory that shows three phases of droplet absorption.[42,47–49] The three phases of the imbibition are described as the increasing drawing area (IDA), constant drawing area (CDA), and decreasing drawing area (DDA). Each phase is categorized by temporal changes in the diameter (=2R) of the drawing area and dynamic contact angles (Fig. 3c and d). Immediately after initiating liquid–solid contact, the droplet undergoes the IDA phase, where 2R increases while the contact angle decreases until it assumes the advancing contact angle.[50] In the sequential CDA phase, the droplet is absorbed into the porous surface at a relatively constant 2R and decreasing contact angle. Once the contact angle assumes the receding contact angle, the droplet is fully consumed (i.e., imbibed) into the media in the DDA phase, decreasing both 2R and contact angle in the process. The segmented NWs with CuO components show drastically different absorption characteristics compared to the Ni NWs (Fig. 3c and d). While all other NWs display rapid transitions through the IDA, CDA, and DDA phases, the droplet on the Ni NW remains pinned to the surface for an extensive time period (≥500 ms), suggesting an innately high spreading resistance in the radial direction (Fig. 3e). Droplets are imbibed into Ni/CuO NWs at the quickest rate (≤4 ms) despite them being more hydrophobic than CuO and CuO/Ni NWs (Fig. 3a). We speculate that the hydrophobicity of Ni NWs at the top direct more liquid towards the superhydrophilic CuO base (Fig. 3d inset) to enhance the wicking effects (Fig. S1†).

Capillary-induced wicking performance

As the next step, we quantify the capillary-assisted liquid transport performance of our segmented NWs by performing a liquid rate-of-rise test. See Experimental section, and Fig. S5.† In brief, when a vertically oriented sample contacts the surface of a liquid pool, a meniscus forms and propagates through the porous media via capillary action (Fig. 4a). The capillary performance parameter defined by permeability over effective pore radius (K/R_{eff}) is obtained from the Lucas–Washburn equation:[33,34,60]

$$h^2 = \frac{4\sigma}{\varphi\mu}\frac{K}{R_{eff}}t \qquad (1)$$

where h is the liquid height, t is the time, μ is the liquid viscosity, $\varphi = 1 - \varepsilon$ is the porosity, and σ is the surface tension of the liquid. The effective pore radius is defined as $R_{eff} = R_p/\cos\theta_s$, where R_p is the pore radius and θ_s is the static contact angle. As expected, the Ni NWs show very low K/R_{eff} values (Fig. 4a), which confirms that the Ni NWs have minimal contributions to capillary-induced liquid transport (Fig. S6†). Furthermore, we observe a trendline that indicates that the K/R_{eff} values of hybrid NWs (i.e., Ni/CuO and CuO/Ni NWs) converge towards the pure CuO NW sample value as the CuO compound ratio increases (Fig. 4b). This phenomenon can mechanistically be explained by primary and secondary wicking motions through the segmented NWs.

As evident in the spreading behaviors (Fig. 3), the segmented NWs possess a unique heterogenous wettability, where the intrinsically opposing wetting characteristics of the two compounds are drastically intensified through nanofeatures. As a result, the liquid wicks through the segmented NWs in primary and secondary phases as shown in Fig. 4c–f. The primary and secondary wicking fronts can be identified through distinctive surface light refraction intensities emitted from the liquid at differing in-plane depths. The primary and secondary wick propagations are quantified through an average grayscale analysis, where pixelwise intensities (i.e., light refraction intensities) are used to locate the primary and secondary wicking fronts (Fig. 4g and h). While all segmented NWs draw liquid in a two-step process, the two-step wicking is only observable in Ni/CuO NWs, owing to the secondary wicking front's position relative to the imaging direction (Fig. 4e; see Movie S1† for real-time visualization of the two-step wicking process). Within the Ni/CuO NWs structures, the secondary wicking is induced by in-plane infiltration mechanisms through the Ni NWs, as illustrated in Fig. 4e and f. The primary wicking occurs in the superhydrophilic CuO NW region and is dictated by microscopic liquid pathways with the

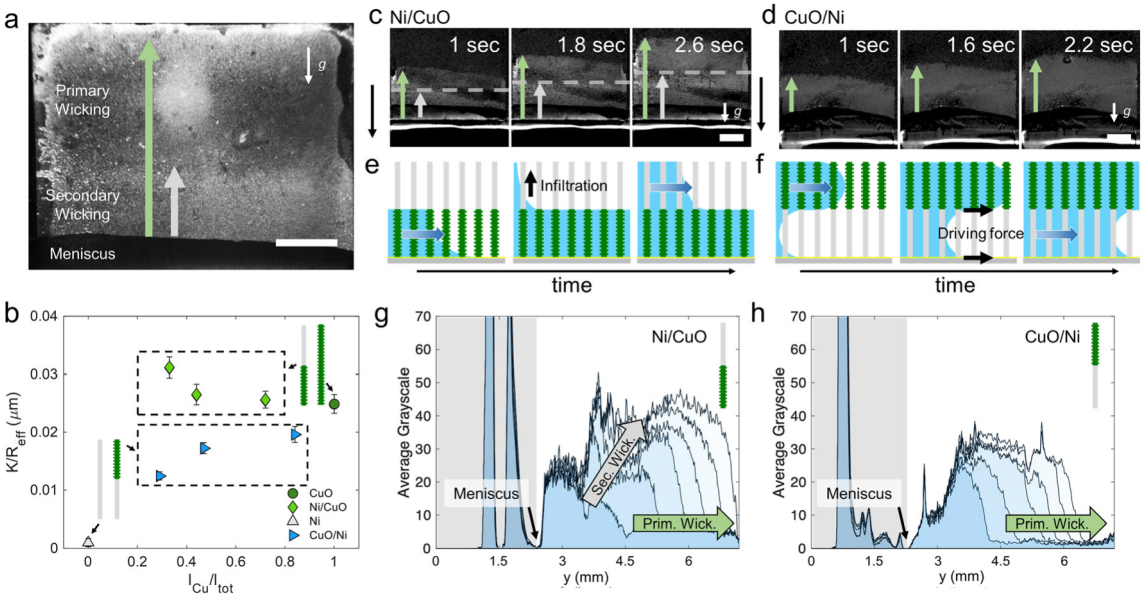

Fig. 4 Capillary-driven wicking performance of NWs. (a) Segmented NWs exhibit unique two-step capillary wicking behaviors with primary and secondary wicking fronts. Liquid rise is captured by a microscopic optical camera at 60 fps. The scalebar is 2 mm. (b) The capillary performance parameter (K/R_{eff}) of the NWs converge towards the CuO NW value as the CuO content increases. The error bars are determined using propagation of error of the measured quantities. Timelapse (c) optical images and (e) illustrations of Ni/CuO NW wicking. The secondary wicking through the Ni NW is primarily due to in-plane liquid infiltration mechanisms. Gray dashed lines indicate the secondary wicking front. Timelapse (d) optical images and (f) illustrations of CuO/Ni NW wicking. The infiltration-induced secondary wicking is assisted by the hydrophilic Au base. The scale bars represent 2 mm. (g) and (h) Changes in the average image grayscale relative to the first frame can visualize primary and secondary wicking. The histogram color fades as time increases. Secondary wicking is identified by increases in the light intensity, which is shown in the plot as vertical upwards histo-gram shifts.

smallest effective wicking distance (Fig. S7†). By reviewing the accrued capillary performance results in Fig. 4b, we speculate that maximum K/R_{eff} is achieved at the superhydrophilic thin CuO base layer shown in Fig. S1.† Since out-of-plane liquid deliver primarily takes place in the CuO portion, Ni/CuO NWs have relatively better capillary performances compared to CuO/Ni NWs (Fig. 4b) due to combined wicking effects from the CuO NWs and the CuO base. We accordingly attribute the maximum K/R_{eff} value for Ni/CuO NWs to CuO base-dominated capillarity at low CuO contents, where this dominance fades as the hydraulic resistance relatively increases with higher l_{cu}/l_{tot} ratios. In contrast to Ni/CuO NWs, CuO/Ni NWs lacks a superhydrophilic base and K/R_{eff} scales as a function of CuO content for CuO/Ni NWs as available CuO liquid transport pathways increase. We emphasize that the reported K/R_{eff} values (0.01–0.03 μm) for segmented NWs is approximately 10× higher than our recently reported high-performance hierarchical nanoscale wick designs.[51,52]

Pool boiling two-phase heat transfer

Having characterized the surface properties of our hierarchical nanostructures, we proceed to quantify the pool boiling heat transfer characteristics. All experiments are conducted on a custom pool boiling setup presented in Fig. S8 and Table S1,† and Experimental section. The boiling properties are measured by the steady-state surface heat flux q″ with respect to superheat $\Delta T = T_s - T_{sat}$, at incrementally increased input heat loads. In the resulting boiling curve (Fig. 5a), the CHF is identified as the local maximum, and the HTC = q″/ΔT is represented by the boiling curve slope.

All NW surfaces display significant HTC and CHF improvements, regardless of the material and composition, in comparison to an unmodified Si surface. A summary of the experimentally measured boiling performances is provided in Table 2. Considering the poor capillary performance of the pure Ni NW, even this surface had a CHF of 79 W cm^{-2}, which is a ⍰150% increase than the unmodified surface, which we attribute to in-plane infiltration-induced liquid delivery mechanisms described in previous sections (Fig. 3 and 4). By implementing the superhydrophilic, hierarchical nanofeatures originated from CuO NWs, we manipulate the curve to achieve even higher CHFs of 105–128 W cm^{-2}, where the enhancement ratio compared to the unmodified surface is 4 (Fig. 5a). Simultaneously, the boiling-curve-averaged HTC, $\bar{h} = \frac{1}{\Delta T_{CHFONB}} \int_{\Delta T_{ONB}}^{\Delta T_{CHF}} h(\Delta T)d(\Delta T)$, shows a 60% and >120% increase for Ni NWs and NWs with CuO content, respectively, compared to the unmodified Si surface. However, a closer inspection reveals an opposite trend at low heat fluxes (q''_{low} <20 W cm^{-2}), where the Ni NW surface achieves the highest q''_{low} region HTC, $\bar{h}_{low} = \frac{1}{\Delta T_{q''_{low}ONB}} \int_{\Delta T_{ONB}}^{\Delta T_{q''_{low}}} h(\Delta T)d(\Delta T)$, enhancement (⍰2.3× higher) compared to the unmodified Si surface (Fig. 5b). Please see section S3 of the ESI† for further

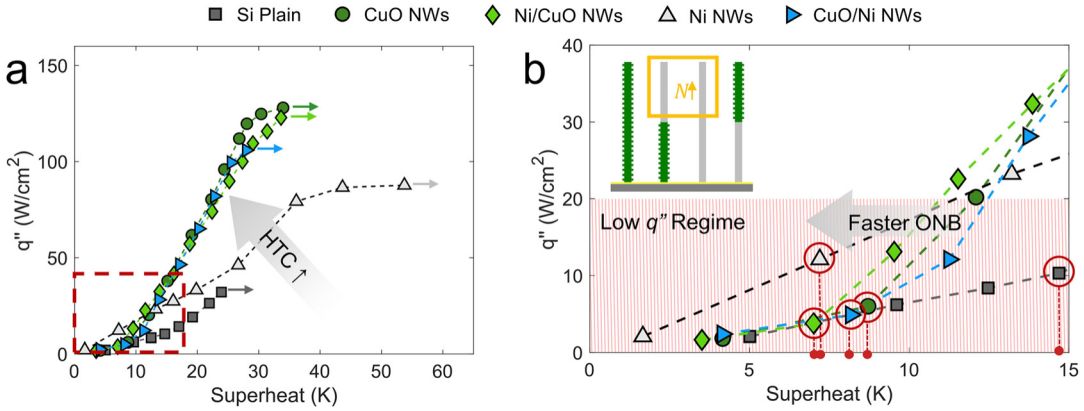

Fig. 5 Pool boiling heat characterization on the structured surfaces. (a) Boiling heat flux (q″) as a function of wall superheat ($\Delta T = T_s - T_{sat}$). The critical heat flux (CHF) is marked with arrows. The boiling curve slope characterizes the heat transfer coefficient (HTC). A representative composition ratio of $l_{CuO}/l_{tot} \approx 0.5$ is selected for hybrid NW pool boiling experiments. The red box represents the (b) zoomed in boiling curve at the low q″ regime. The onset of nucleate boiling (ONB) is circled in red and marked in the x-axis for clarity. The inset illustrates the effectiveness of Ni-top NWs at facilitating bubble nucleation and increasing bubble numbers. Error bars are not shown for clarity. For a detailed discussion and quantification of measurement error, please see section S2 of the ESI.†

Table 2 Summary of experimentally measured boiling heat transfer performances

Surface type	h ($W\,cm^{-2}\,K^{-1}$)	h_{low} ($W\,cm^{-2}\,K^{-1}$)	CHF ($W\,cm^{-2}$)	χ	ψ
Si plain	1.09	0.74	32.1	1	1
CuO NWs	3.47	1.14	128.08	1.54	3.9
Ni/CuO NWs	3	1.23	122.93	1.66	3.82
Ni NWs	1.73	1.71	79.25	2.30	2.46
CuO/Ni NWs	2.39	1.01	105.93	1.37	3.3

description of q''_{low}. Moreover, the NWs with Ni content show advanced boiling incipience (i.e., ONB), which implies that these surfaces can operate under the more efficient nucleate boiling regime at earlier stages. As expected, the Ni/CuO NW surface proposed to take advantages of both Ni and CuO contents performs exceedingly well on both ends of the boiling curve, with a 175% increase of h, a 70% increase of h_{low}, a 283% increase of CHF, and a 52% earlier ONB compared to the control Si surface.

The further demonstration of a deep learning-based computer vision framework (i.e., VISION-iT) enables us to study how the stunning variety of collective structure-dependent bubble nucleation behaviors regulate the boiling performances. VISION-iT chiefly employs object detection, object tracking, and data processing (Fig. S9a†), to autonomously curate >100 000 rich, physical descriptors (position, size, frequency, distribution, etc.) per dataset from boiling images at single-bubble resolution. The object detection module identifies and labels every bubble per image with instance-specific pixel-wise masks, where each mask is assigned a unique identifier (ID). Then, the IDed masks are linked together with respect to time through k-dimensional (k-d) tree algorithms in an object tracking module. The tracked spatio-temporal features are finally post-processed to extract features such as the departure bubble diameter D_b, the bubble departure frequency f_b, and nucleation site density N_b. A more detailed description of the framework can be found in ESI S3† and previous work.[39] The model performance and training procedures are documented in the Experimental section.

According to mechanistic pool boiling models,[53–61] D_b, f_b, and N_b, are key parameters used to partition the heat flux into natural convection q''_{nc}, evaporation q''_{ev}, and bubble departure-driven forced convection q''_{fc} heat transfer modes, see ESI section S3.2. and eqn (S13)–(S16).† The departure bubble diameter D_b is indicative of the vapor production rate and is governed by buoyant and surface tension forces acting on the bubble.[62] When D_b is small, boiling heat transfer is determined by a balance between f_b and N_b. For example, the heat flux of a surface with high f_b but low N_b may be governed by q''_{nc} due to the large effective non-bubble-influenced area $A_{nbi} = (1 - N_b\pi D_b^2/4)$ exposed to natural convection. When D_b is large, q''_{nc} naturally reduces and the heat transfer is gradually dictated by q''_{ev} as it scales with D_b^3. Therefore, it is imperative to acquire D_b, f_b, and N_b to understand the underlying mechanisms that govern boiling heat transfer in the proposed NW designs. See ESI S3† for bubble detection algorithm details and Table S2† for extracted bubble parameters.

Past studies have shown evidence that the bubble statistics at the ONB can serve as good indicators of the CHF because it is a representative stage where the heat transfer mode changes from single-phase natural convection to nucleate pool boiling.[25,63] We expand this notion to see whether the ONB boiling parameters can be used to shed light on mechanisms governing the HTC as well. Since the HTC is an ever-evolving parameter highly governed by bubble dynamics, we restrict the study scope to h_{low}, where the bubble dynamics show main characteristics of the ONB. The side-view bubble evolution processes near the ONB of all samples are shown in Fig. 6a–e, where tracked bubbles are overlayed with pixel-wise masks (see Movie S2† for real-time videos). Extracted bubble statistics

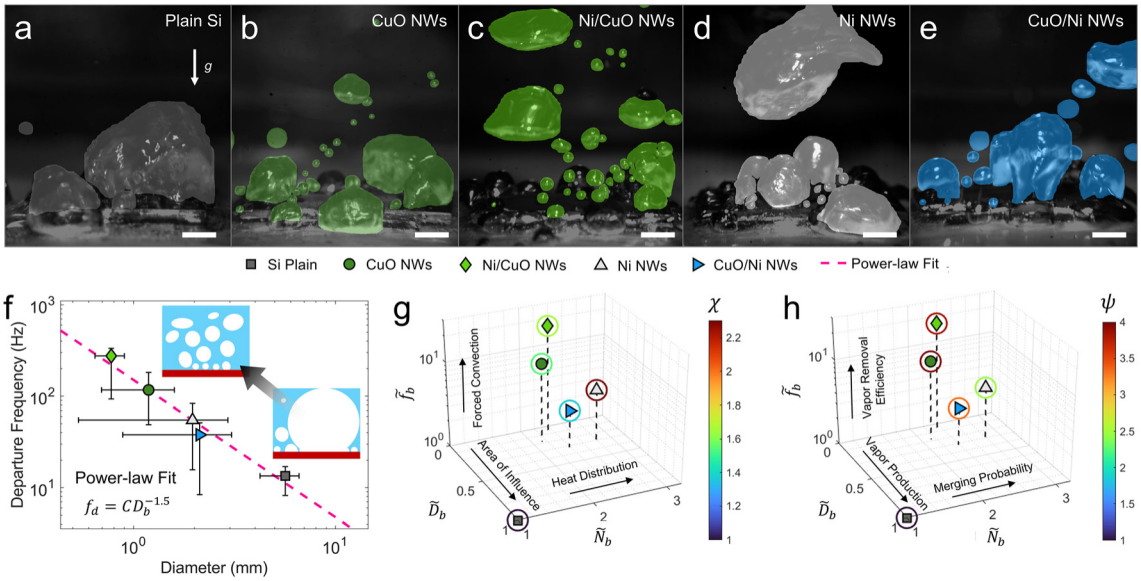

Fig. 6 Bubble nucleation and departure behavior on unmodified and modified surfaces near the ONB. Representative side-view high-speed optical images of tracked bubbles on (a) plain Si (which is the unmodified surface), (b) CuO NW, (c) Ni/CuO, (d) Ni, and (e) CuO/Ni surfaces. The masks are color-coded with respect to the surface type. The scale bar is 2 mm. (f) Bubble departure frequency (f_d) as a function of departure bubble diameter (D_b) shows that that f_d scales with $D_b^{1.5}$. The error bar represents the 16th and 84th percentile point, meaning that 68% of the datapoints lie within the error bar range. The inset illustrates how bubble characteristics change as a function of f_d and D_b. The bubble statistics are gathered from approximately 130–200 bubbles at the ONB ($q'' = 3–12$ W cm^{-2}). Four-dimensional plot of the (g) HTC enhancement ratio ($\chi = h_{low,modified}/h_{low,-unmodified}$) at low (<20 W cm^{-2}) heat fluxes and (h) CHF enhancement ratio ($\psi = CHF_{modified}/CHF_{unmodified}$) as a function of bubble departure frequency ratio ($f_b = f_{b,modified}/f_{b.unmodified}$), departure diameter ratio ($D_b = D_{b,modified}/D_{b,unmodified}$), and effective nucleation site density ratio ($N_b = N_{b,modified}/ N_{b,unmodified}$). The enhancements are represented with colored circles around the marker.

shows that f_b scales with $D_b^{1.5}$ (Fig. 6f), which is a byproduct of the surface compensating for smaller bubbles by ejecting them at faster rates to balance heat removal. The error bars represent the 16th and 84th percentile of the data, meaning that 68% of the datapoints reside within the error bar range.

The bubble statistics (from approximately 130–200 bubbles at the ONB) reiterate the importance of engineering wettability for optimal bubble activities. On the one hand, surfaces with wettable bases (i.e., Ni/CuO and CuO NW surfaces with CuO at the bottom) display orders of magnitude higher f_b than the unmodified Si surface, demonstrating superior vapor removal capacities. On the other hand, surfaces with non-wettable bases (i.e., Ni and CuO/Ni NW with Ni at the bottom) display a >2× wider D_b distribution than the CuO NW surface, suggesting a systemic failure of the surface to rid itself of small bubbles. Despite having surface properties favorable for bubble nucleation, the delayed wetting of the hydrophobic Ni NWs hinders bubble departure when positioned at the sample base. Based on the acquired bubble statistics, we thus infer that f_b is governed by the NW's base wettability, where bottom pressure fields generated by the out-of-plane wicking is speculated to help detach bubbles forming on the top. The bare Si surface show the overall poorest bubble evolution and departure behaviors, with low f_b and large, narrowly distributed D_b. The authors speculate that such pressure gradients caused by the opposing wettability of the segmented NWs can suppress or encourage bubbles, resulting in the ONB trend in Fig. 5b.

VISION-iT allows us to further quantify the multi-dimensional relationship between boiling parameters, heat transfer performances, and structural design, by defining non-dimensional HTC and CHF enhancement ratios compared to the unmodified Si, $\chi = h_{low,modified}/h_{low,unmodified}$ and $\psi = CHF_{modified}/CHF_{unmodified}$, respectively. Fig. 6g and h shows four-dimensional (4D) maps of χ and ψ, with respect to departure diameter ratio ($\tilde{D}_b = D_{b,modified}/D_{b,unmodified}$), departure frequency ratio ($\tilde{f}_b = f_{b,modified}/f_{b.unmodified}$), and nucleation site density ratio ($\tilde{N}_b = N_{b,modified}/N_{b,unmodified}$), where χ and ψ are represented as the fourth dimension with a color-mapped circle. The subscripts modified and unmodified indicate the nanostructures (nanowires in this study) and the bare silicon substrate.

A summary of the boiling performance enhancements is provided in Table 2. From the boiling efficiency perspective (Fig. 6g),[60,61] χ (i.e., HTC ratios at low heat flux) mechanistically depends on liquid perturbation-induced forced convection at the wake of bubble departure (i.e., $\tilde{f}_b$), the area of influence (i.e., $\tilde{D}_b$), and the heat transfer distribution along the surface (i.e., $\tilde{N}_b$). The influence of $\tilde{f}_b$ is conspicuous in Fig. 6g, where the χ of surfaces with similar $\tilde{N}_b$ or $\tilde{D}_b$ are ranked following the order of $\tilde{f}_b$. However, $\tilde{N}_b$ likely dominates HTC at low heat fluxes by observing that the Ni NW surface has the highest χ of 2.3 despite having 80% lower f_b than the Ni/CuO NW surface. The findings elucidate that at early boiling stages ($q'' < 20$ W cm^{-2}), it is necessary to design the boiling surface to dissipate heat evenly, rather than aggressively to maximize heat transfer.

From the boiling crisis standpoint (Fig. 6h),[60,61] ψ relies on the quantity of vapor generation (i.e., $\tilde{D}_b$), vapor removal efficiencies (i.e., $\tilde{f}_b$), and merging probabilities (i.e., $\tilde{N}_b$). While the unmodified surface is primarily limited by vapor removal deficiencies and excessive vapor production, the NWs are restricted by a combination of $\tilde{D}_b$, $\tilde{f}_b$ and $\tilde{N}_b$. For example, the bubbles on the surfaces with non-wettable bases (i.e., Ni NW and CuO/Ni NW surfaces with Ni at the bottom) tend to form with high nucleation densities, but depart with low frequencies. The tendency for a dense batch of bubbles with poor detachment capabilities to form naturally leads to increased bubble-bubble interactions, ultimately resulting in relatively large bubbles, which can potentially trigger the CHF.[63] In contrast, the surfaces with wettable bases (i.e., CuO and Ni/CuO NW surfaces with CuO at the bottom) proficiently remove vapor thermal barriers from the surface at reasonable nucleation densities and are hence assumed to be capable of sustaining higher heat loads.

Discussion

Achieving high HTC and CHF have conflicting requirements on the surface morphological and chemical properties. The CuO NW surface is an excellent example of how hierarchical structures with ultra-rough, superhydrophilic surface properties have been able to achieve high boiling performances in both aspects. Our work further pushes the limit of traditional hierarchical surface designs by combining two distinct surface properties into one nanoarchitecture, thereby tailoring the design for efficient vapor and liquid pathways during pool boiling. The liquid rate-of-rise tests and SEM characterization confirm the existence of superhydrophilic nanofeatures at the base of Ni/CuO and CuO NWs. Our results suggest that the base wettability of structures fabricated should be taken into consideration in future research and could even be potentially used to address grain boundary-induced hydraulic resistance in 3D architectures created using similar techniques.[52,64,65] Furthermore, our work shows that the hierarchical NWs retain exceptional capillary performance (i.e., K/R_{eff}), even when combined with non-wicking Ni NW arrays. As a result, our hybrid Ni/CuO NW surface not only achieves 175% and 282% increases in HTC and CHF, respectively, when compared to an unmodified plain Si surface, but also improves the HTC at low-heat flux ranges by 8% and advances the ONB by 20% compared to the cutting-edge hierarchical CuO NW surface, while maintaining same levels of CHF performance.

Furthermore, the developed deep learning-based computer vision framework (VISION-iT) enables greater mechanistic understanding of the boiling process by connecting heat transfer and the large spatiotemporal bandwidth of bubble statistics. Here, the autonomous curation of massive in situ bubble datasets enabled by our framework stands to compliment recent advances in imaging techniques, that exclusively study top- and bottom-view bubble statistics to identify the fundamental physics governing pool boiling.[58,59,66,67] The datasets acquired at the ONB confirmed the correlations between bubble statistics and heat transfer performances. Due to the multidimensionality of the problem, innate structural heterogeneity of the hybrid NWs, and intrinsic variability of pool boiling experiments, still it is challenging to precisely predict overall HTC and CHF. As shown in Fig. S9,† the variability of the pool boiling curves may easily vary 10% or more. However, previous work has demonstrated that the changes in the boiling curve will be reflected in the bubble statistics.[38] To clarify these questions, future research will include a systematically designed parametric study of bubble dynamics throughout the entire boiling curve.

In conclusion, our results confirm our hypothesis that boiling surfaces can be enhanced for both high-and-low heat flux applications through a synergistic cooperation of hierarchical architecture and heterogeneous vertical wettability, showing the potential for the further optimization. The combined efforts of surface chemistry, materials science, thermal engineering, and deep learning techniques shed light on the mechanistic relationship between vapor/liquid pathways, bubble statistics, and overall heat and mass transfer performance. Our proposed surface and characterization methods will help pave new design guidelines for other energy applications including boiling, condensation, thin-film evaporation, and microscopic liquid transport devices.

Experimental

Fabrication and surface modification

Fabrication of the segmented nanowires is composed of three steps: (1) substrate preparation, (2) templated electrodeposition of metals, and (3) surface modifications. First, a Ti/Au (5/50 nm) layer is deposited via evaporation on a 12 mm × 12 mm Si subtrate. The Cu layer is additionally deposited onto the backside of the substrate using an E-beam evaporator. The substrate of choice for fabricating of segmented NWs must be smooth, hydrophilic, corrosion resistant, and electroconductive. The nanowires are fabricated via electrodeposition using a sacrificial track-etched polycarbonate membrane. The membrane thickness is 30 μm and consists of pore diameters of approximately 1000 nm. Metals (Cu and Ni) are then electrodeposited in an electrochemical cell containing electrolyte that is confined by an equally sized aperture. For deposition, a constant voltage of V = −320 mV (Ag/AgCl) and V = −1100 mV (Ag/AgCl) for Cu and Ni is applied, respectively. The electrolyte is composed of 0.6 M $CuSO_4$ + 30 mM H_2SO_4 for Cu deposition and 1 M $NiSO_4$ + 0.2 M $NiCl_2$ + 0.6 M H_3BO_3 for Ni Deposition. It should be noted that we intentionally underfill the template to render NW lengths of 20 μm in order to prevent overfilling-induced surface nonuniformities. The as-fabricated nanowires are further treated by selective surface oxidation after resolving the sacrificial template in Dichloromethane (Sigma Aldrich, >99V) for 1.5 h at 40 °C on the hot plate. The surface oxidation is treated by immersing nanowires in a preheated alkaline solution that is composed of a 1.7 M $NaClO_2$ (Sigma Aldrich,

>99%) and a 0.25 M NaOH (Sigma Aldrich, >98% pellet) for 2 min. The immersion time is chosen based on past work, where the CuO nanostructures are shown to achieve stability in both growth and hydrophilicity after 60 s.[29] Finally, the nanowires are sequentially cleaned using deionized water, isopropyl alcohol, and acetone.

Surface characterization

Morphological details of the nanowires are investigated using FEI Magellan 400 SEM at a 15 kV of accelerating voltage for both measurement from top view and cross-sectional view. To capture the cross-sectional images, the nanowires are cleaved and mounted on a vertical sample mount. Surface wetting properties are investigated via contact angle measurements using a sessile droplet method with a goniometer (MCA-3, Kyowa, Interface Sciences). Because droplets are almost instantaneously fully consumed into surfaces with extreme wicking capabilities (Fig. 3d), we measure the apparent advancing CA (θ_{app}) of droplets the moment that they retain stable spherical cap shapes on the surface. The goniometer dispenses a 15 nL deionized water droplet from a 30 μm diameter capillary tip, assisted by constant air pressure (12 kPa). The droplet behavior during surface impact is captured by a side-view high-speed microscopic camera to measure contact angle (5000 fps), and by a top-view optical microscope to record droplet infiltration and spreading dynamics (30 fps). The contact angle is evaluated by averaging results from three individual measurements in different surface locations.

Liquid rate-of-rise test

The NW wicking performance is evaluated by the liquid rate-of-rise test (Fig. S5†), which calculates capillary performance parameters using the eqn (1). The liquid rate-of-rise test is performed in a saturated chamber with a water reservoir to prevent undesired evaporation during the test. The water reservoir is sealed with a parafilm for at least one week ahead of the test. The liquid rise is captured at 60 fps using a high-speed optical camera with a LED lighting source.

Pool boiling test

Pool boiling heat transfer of the nanowires is experimentally investigated using a custom-built pool boiling experimental setup (see Fig. S8 and ESI S3† for details). The pool boiling setup is composed of chamber, data acquisition system, copper block and heaters. The boiling chamber is composed of lid and transparent polycarbonate wall to capture the bubble dynamics using the high-speed camera (FASTCAM Mini AX50) at 2000 fps with LED lighting source. Heat flux and surface temperature in boiling test are calculated from the temperature results obtained from data acquisition system (LabJack U6) connected to four K-type thermocouples to read temperatures of the copper block. Thermal energy is generated from the four cylindrical cartridge heaters (Omega, CIR-20191) that are inserted at the bottom of the copper block. Glass wool insulation is wrapped around the copper block to minimize heat loss to the ambient environment and to promote one-dimensional heat conduction toward the sample. The heat flux is controlled by slowing increasing power using voltage transformer (Variac AC variable voltage converter). Before the boiling test, sample is placed and attached on the 1 cm × 1 cm copper block through soldering. Once the sample is firmly fixed on the copper block with proper PDMS sealing, the chamber is filled with working fluid (DI water). To maintain the water temperature close to saturation temperature, a guard heater that is connected to proportional integral derivative controller is used and immersed in the water.

Pool boiling model training and evaluation

We train a deep neural net object detector (i.e., Mask R-CNN) that generates pixel-wise masks for every object in an image. The object detection model trains on a custom-built image inventory of manually labeled bubble images gathered through years of experiments. To diversify the training data, we implement image augmentation techniques, which randomly transforms the original data into new, slightly modified versions. The total augmented training dataset (6944 images) are split into 80% (5555 images) train and 20% (1389 images) test sets. The model trains for a total of 100 epochs using stochastic gradient descent with a learning rate of 1e-3 and momentum of 0.9. The training results are presented in Fig. S9b,† showing that both train and test losses drop considerably low with a test loss of ⍰0.08, which indicates successful learning. Our model performs exceptionally well (> 90%) on traditional evaluation metrics such as recall, precision, accuracy, and F1-score (see ESI section S3, Fig. S10, and S11† for detailed evaluation of model performance). Furthermore, we report a pixel-wise mean average percentage error (MAPE) of 1.56% and an occlusion-induced error (OIE) of approximately 4.6% (Fig. S9c†). We attribute the small OIE errors to the relatively small (1.2 × 1.2 cm) boiling surface dimension. It should be noted that the spatial resolution of predicted masks is dictated by the lens magnification and imaging framerate used in the analysis. For this study, we report a minimum detected bubble size of D_b ⍰0.2 mm. While not applicable for bubbles at ONB, the maximum detectable bubble size limited by the viewing window size is estimated to be D_b ⍰10.8 mm.

Author contributions

J.L. and Y.S. contributed equally to this work. J.L. and Y.S. performed research; J.L. and M.K. prepared the samples; J.L. conducted the experiments; Y.S. analyzed the data, developed the theory, and developed the computational framework; Y.S. and P.S. evaluated the model performance; Y.W. proposed and supervised the project; and J.L., Y.S., P.S., M.K., M.T.B., and Y.W. wrote the paper. All the authors participated in discussion of the research.

Conflicts of interest

There are no conflicts to declare.

Acknowledgements

This work was sponsored by the National Science Foundation (NSF) (Grant No. CBET-TTP 2045322, Thermal Transport Processes). J. L. and Y. S. are grateful for the financial support from the UC Irvine Mechanical and Aerospace Engineering Department Graduate Fellowship and support received through the collaborated work with Northrop Grumman Basic Research Center. Material characterizations were performed at the UC Irvine Materials Research Institute (IMRI).

References

1 H. J. Cho, D. J. Preston, Y. Y. Zhu and E. N. Wang, Nat. Rev. Mater., 2017, 2, 1–17.
2 R. Chen, M. C. Lu, V. Srinivasan, Z. Wang, H. H. Cho and A. Majumdar, Nano Lett., 2009, 9, 548–553.
3 K. H. Chu, Y. S. Joung, R. Enright, C. R. Buie and E. N. Wang, Appl. Phys. Lett., 2013, 102, 151602.
4 T. J. Hendricks, S. Krishnan, C. H. Choi, C. H. Chang and B. Paul, Int. J. Heat Mass Transfer, 2010, 53, 3357–3365.
5 S. G. Kandlikar, J. Heat Transfer, 2001, 123, 1071–1079.
6 J. Kim, Int. J. Multiphase Flow, 2009, 35, 1067–1076.
7 C. Li and G. P. Peterson, J. Heat Transfer, 2007, 129, 1465–1475.
8 C. Li, Z. Wang, P. I. Wang, Y. Peles, N. Koratkar and G. P. Peterson, Small, 2008, 4, 1084–1088.
9 H. O'Hanley, C. Coyle, J. Buongiorno, T. McKrell, L. W. Hu, M. Rubner and R. Cohen, Appl. Phys. Lett., 2013, 103, 024102.
10 A. K. Rajvanshi, J. S. Saini and R. Prakash, Int. J. Heat Mass Transfer, 1992, 35, 343–350.
11 R. L. Mohanty and M. K. Das, Renewable Sustainable Energy Rev., 2017, 78, 466–494.
12 N. H. Fletcher, J. Chem. Phys., 1958, 29, 572–576.
13 S. F. Jones, G. M. Evans and K. P. Galvin, Adv. Colloid Interface Sci., 1999, 80, 27–50.
14 Y. T. Mu, L. Chen, Y. L. He, Q. J. Kang and W. Q. Tao, Int. J. Heat Mass Transfer, 2017, 106, 708–719.
15 A. R. Betz, J. Jenkins, C. J. Kim and D. Attinger, Int. J. Heat Mass Transfer, 2013, 57, 733–741.
16 H. J. Cho, J. P. Mizerak and E. N. Wang, Nat. Commun., 2015, 6, 1–7.
17 H. J. Jo, H. S. Park and M. H. Kim, Int. J. Heat Mass Transfer, 2016, 93, 554–565.
18 M. M. Rahman and M. McCarthy, Heat Transfer Eng., 2017, 38, 1285–1295.
19 R. F. Wen, Q. Li, W. Wang, B. Latour, C. H. Li, C. Li, Y. C. Lee and R. G. Yang, Nano Energy, 2017, 38, 59–65.
20 Q. N. Pham, Y. Suh, B. Shao and Y. Won, Int. Electron. Packag. Tech. Conf. Exhib., 2019, 59322.
21 Q. N. Pham, S. W. Zhang, S. Hao, K. Montazeri, C. H. Lin, J. Lee, A. Mohraz and Y. Won, ACS Appl. Mater. Interfaces, 2020, 12, 19174–19183.
22 Y. Suh, C.-H. Lin, H. Gowda and Y. Won, International Electronic Packaging Technical Conference and Exhibition, 2019, 59322, V001T01A001.
23 X. Yuan, Y. Du and J. Su, Renewable Sustainable Energy Rev., 2022, 156, 111974.
24 K. H. Chu, R. Enright and E. N. Wang, Appl. Phys. Lett., 2012, 100, 151602.
25 J. Q. Li, W. C. Fu, B. H. Zhang, G. H. Zhu and N. Miljkovic, ACS Nano, 2019, 13, 14080–14093.
26 S. Shin, G. Choi, B. Rallabandi, D. Lee, D. Il Shim, B. S. Kim, K. M. Kim and H. H. Cho, Nano Lett., 2018, 18, 6392–6396.
27 D. Lee, N. Lee, D. Il Shim, B. S. Kim and H. H. Cho, Appl. Therm. Eng., 2018, 130, 710–721.
28 J. Lee, B. Shao and Y. Won, IEEE Trans. Compon., Packag., Manuf. Technol., 2018, 9, 1075–1081.
29 J. Lee, Y. Suh, P. P. Dubey, M. T. Barako and Y. Won, ACS Appl. Mater. Interfaces, 2019, 11, 1546–1554.
30 Y. Suh, C. H. Lin, H. Gowda and Y. Won, J. Electron. Packag., 2020, 142, 031105.
31 B. Bourdon, R. Rioboo, M. Marengo, E. Gosselin and J. De Coninck, Langmuir, 2012, 28, 1618–1624.
32 B. Bourdon, E. Bertrand, P. Di Marco, M. Marengo, R. Rioboo and J. De Coninck, Adv. Colloid Interface Sci., 2015, 221, 34–40.
33 D. Lim and I. C. Bang, Int. J. Heat Mass Transfer, 2020, 150, 119360.
34 W. T. Hsu, D. Lee, N. Lee, M. Yun and H. H. Cho, Int. J. Heat Mass Transfer, 2021, 164, 120596.
35 J. Lee, J. So, W. G. Bae and Y. Won, Adv. Mater. Interfaces, 2020, 7, 1902150.
36 A. Jaikumar and S. G. Kandlikar, Int. J. Heat Mass Transfer, 2016, 95, 795–805.
37 Y. Q. Wang, J. L. Luo, Y. Heng, D. C. Mo and S. S. Lyu, Int. Commun. Heat Mass Transfer, 2020, 111, 104441.
38 Y. Suh, R. Bostanabad and Y. Won, Sci. Rep., 2021, 11, 1–10.
39 Y. Suh, J. Lee, P. Simadiris, X. Yan, S. Sett, L. N. Li, K. F. Rabbi, N. Miljkovic and Y. Won, Adv. Sci., 2021, 8, 2101794.
40 M. T. Barako, S. G. Isaacson, F. F. Lian, E. Pop, R. H. Dauskardt, K. E. Goodson and J. Tice, ACS Appl. Mater. Interfaces, 2017, 9, 42067–42074.
41 M. T. Barako, S. Roy-Panzer, T. S. English, T. Kodama, M. Asheghi, T. W. Kenny and K. E. Goodson, ACS Appl. Mater. Interfaces, 2015, 7, 19251–19259.
42 F. Blanchette and T. P. Bigioni, Nat. Phys., 2006, 2, 254–257.
43 J. Bico, U. Thiele and D. Quere, Colloids Surf., A, 2002, 206, 41–46.
44 E. Chibowski and R. Perea-Carpio, Adv. Colloid Interface Sci., 2002, 98, 245–264.
45 A. B. D. Cassie and S. Baxter, Trans. Faraday Soc., 1944, 40, 0546–0550.
46 R. N. Wenzel, Ind. Eng. Chem., 1936, 28, 988–994.
47 N. ContetAudonneau, J. L. Schmutz, A. M. Basile and C. deBievre, Eur. J. Dermatol., 1997, 7, 115–117.
48 L. Courbin, J. C. Bird, M. Reyssat and H. A. Stone, J. Phys.: Condens. Matter, 2009, 21, 464127.
49 A. S. Kousalya, J. A. Weibel, S. V. Garimella and T. S. Fisher, Int. J. Heat Mass Transfer, 2013, 59, 372–383.

50 M. Hilpert and A. Ben-David, Int. J. Multiphase Flow, 2009, 35, 205–218.
51 Q. N. Pham, B. Shao, Y. Kim and Y. Won, ACS Appl. Mater. Interfaces, 2018, 10, 16015–16023.
52 Q. N. Pham, M. T. Barako, J. Tice and Y. Won, Sci. Rep., 2017, 7, 10465.
53 R. Benjamin and A. Balakrishnan, Int. J. Heat Mass Transfer, 1996, 39, 2495–2504.
54 C. Gerardi, J. Buongiorno, L. W. Hu and T. McKrell, Int. J. Heat Mass Transfer, 2010, 53, 4185–4192.
55 R. W. Graham and R. C. Hendricks, NASA Tech. Note, 1967, No. NASA-TN-D-3943.
56 C.-Y. Han, Doctoral Dissertation, Massachusetts Institute of Technology, 1962.
57 R. Judd and K. Hwang, J. Heat Transfer, 1976, 98, 623–629.
58 M. Kim and S. J. Kim, Int. J. Heat Mass Transfer, 2020, 163, 120453.
59 S. H. Kim, G. C. Lee, J. Y. Kang, K. Moriyama, H. S. Park and M. H. Kim, Int. J. Heat Mass Transfer, 2016, 102, 756–765.
60 B. Mikic and W. Rohsenow, J. Heat Transfer, 1969, 91, 245–250.
61 M. Z. Podowski, A. Alajbegovic, N. Kurul, D. Drew and R. Lahey Jr., Mechanistic modeling of CHF in forced-convection subcooled boiling, Knolls Atomic Power Lab., Schenectady, NY, United States, 1997.
62 L. N. Zhang, S. Gong, Z. M. Lu, P. Cheng and E. N. Wang, Int. J. Heat Mass Transfer, 2021, 165, 1–32.
63 N. Zuber, Doctoral Dissertation, University of California, 1959.
64 Y. Suh, Q. Pham, B. W. Shao and Y. Won, Small, 2019, 15, 1804523.
65 Y. J. Suh, H. Gowda and Y. J. Won, J. Colloid Interface Sci., 2020, 576, 195–202.
66 J. Q. Li, D. Kang, K. F. Rabbi, W. C. Fu, X. Yan, X. L. Fang, L. W. Fan and N. Miljkovic, Sci. Adv., 2021, 7, 26.
67 P. Zhou, S. Y. Hua, C. Gao, D. F. Sun and R. H. Huang, Int. J. Heat Mass Transfer, 2021, 174, 121295.